Attraction of Rotors to the Pulmonary Veins in Paroxysmal Atrial Fibrillation: A Modeling Study

Conrado J Calvo, Makarand Deo, Sharon Zlochiver, José Millet, Omer Berenfeld

SUPPLEMENTAL MATERIAL

CONTENT

NON-STANDARD ABBREVIATIONS AND ACRONYMS

AP: Action potential

APD: Action potential duration

AF: Atrial fibrillation

Condition I: All currents varied spatially in the model.

Condition II: All currents, except I_{K1}, varied spatially in the model

Condition III: Only I_{K1} varied spatially in the model

CRN-K: Courtemanche-Ramirez-Nattel and Kneller model of the human atrial cell kinetics

CV: Conduction velocity

DF: Dominant frequency

dV/dt_{max}: Maximum upstroke velocity

ERP: Effective refractory period

G_x: Maximum conductance of channel x

$h \times j$: The fraction of sodium channels available for activation

$h \times j_{peak}$: The maximum fraction of sodium channels available for activation during a cycle

I_{K1}: Inward rectifier potassium current

$I_{K,ACh}$: Acetylcholine modulated inward rectifier potassium current

I_{Kr}: Rapid delayed rectifier potassium current

I_{Ks}: Slow delayed rectifier potassium current

I_{to}: Outward transient potassium current

I_{Na}: Sodium current

I_{CaL}: L-type calcium current

I-V: Relationship between the current density and transmembrane voltage

LA: Left atrium

LV: Left ventricle

MDP: Minimum diastolic transmembrane potential

PVs: Pulmonary veins

PV-LAJ: LA and PV junction

RV: Right ventricle

SP: Singularity point. Used to indicate the pivoting location of a rotor

S1, S2: Two sequential stimulations at particular times and locations

TSP: Time-space plot

DETAILED METHODS

Structural Models

Numerical simulations were performed on 2- and pseudo 3-dimensional structures of the area of transition between the LA and the PV (see Fig. 1) with increasing anatomical realism as:

1. A 50×50 mm^2 regular 2D square model was implemented by no-flux boundary conditions.
2. A pseudo-3D cylindrical surface model constructed by applying no-flux boundary conditions at the LA and PV edges and periodic boundary conditions on the other two edges of a regular 2D mesh.
3. A pseudo-3D funnel-shaped surface was constructed with near-equilateral triangulated mesh with no-flux conditions on the wide (LA) and narrow (PV) edges. The height of the funnel model was set to 30 mm and its diameter was set to increase exponentially from 10 mm at the PV to 48 mm at the LA edges (see Fig. 1) (1). Our LA-PVJ funnel model represents a typical right superior PV as described by (1). The radii of the PV and LA where selected such that the radius at the ostia location (15 mm from the LA-end) is where the 50% Boltzmann factor was placed. The funnel-like geometry model was generated by circumscribing an exponent function around the central axis of the LA-PVJ. Accordingly we created the shape of the funnel with the radius r as a function of the distance from the PV edge as: $r = R + A*\exp(z/B)$, (R, A and B are distance constants) where z, the distance along that axis, was increased with a non-uniform steps that maintained the distance between the rings on the surface of the funnel ($\Delta z^2 + \Delta r^2$) approximately constant. Following, the 3D set of nodes was meshed using the Delaunay triangulation scheme resulting in a quasi-equilateral triangular connectivity with an average intermodal distance of 0.1 mm and standard deviation of less than 0.01 mm.

Ionic Modeling

The transmembrane potential at each node was based on the Courtemanche-Ramirez-Nattel and Kneller (CRN-K) model of human atrial cell kinetics in the presence of acetylcholine (ACh) (2-4). I_{KACh} kinetics was based on the formulation by Kneller et al (3) with a minimal amount of [ACh]=0.0015 μM to enable rotors in the CRN model of the atria (4):

$$I_{K,ACh} = \left(\frac{10}{1+\frac{9.12652}{[ACh]^{0.477811}}}\right)\cdot\left(0.013384+\frac{0.22663}{1+\exp\left(\frac{V+80.253}{50.714}\right)}\right)\cdot(V-E_K) \qquad \text{(Eq. 1)}$$

where V (mV) is the transmembrane potential and E_K (mV) is the potassium reversal potential. Compatibility of action potentials calculated at 1 Hz pacing between this study and those by Kneller et al (3) was confirmed. In the simulations presented in Fig. S6, the formulation for I_{K1} based on the Kir2.1 or Kir2.3 isoforms was as reported by Dhamoon et al (5) and differing from the CRN-K model (2-3):

$$I_{K1} = a_4 + \frac{a_1\cdot(V-E_K)}{a_2+\exp[a_3\cdot(V-E_K)]}\,. \qquad \text{(Eq. 2)}$$

Table ST1 contains values of the a_1-a_4 parameters in Eq. 2 fitted for I_{K1} consisting of either Kir2.1 or Kir2.3 isoforms (5):

Table ST1. Coefficients for data fitted for Kir2.1 and Kir2.3 in the I_{K1} of Eq. 2. (5)

Current (isoform)	**Coefficient**	**Value**
I_{K1} (Kir2.1)	a_1	0.4719
	a_2	7.1202
	a_3	0.1187
	a_4	0.0
I_{K1} (Kir2.3)	a_1	0.048
	a_2	0.0333
	a_3	0.2227
	a_4	-0.0607

Simulations and Conditions

Electrical activity was coded in C and MPI and computed on the Flux High Performance Computing cluster at the University of Michigan using a mono-domain, finite volume discretization (FVM), Euler forward scheme with 100 µm internodal distance (h), 0.005 ms time step (Δt), and isotropic diffusion coefficient of 0.062 mm^2/ms (D) adjusted for conduction velocity (CV) of 48 cm/s. Numerical stability of the solutions was assured. During propagation neither irregular (squared, mesh affected) wavefront curvature nor instability of the action potentials, nor any numerical artifacts were observed. Additionally, we verified that our simulations parameters satisfy the 2-dimensional Nyquist stability criterion (6): $D \cdot \Delta t/h^2 < 1/(2 \cdot \text{dimensions})$ which yields $0.031 < 0.25$. Initial conditions were the steady state membrane variables following pacing a single cell at 1 Hz for 10 s.

Heterogeneous ionic conditions were implemented by assigning a spatial Boltzmann ($x_{1/2}$ = 25 mm and Δx = 5 mm) distribution of conductance for I_{K1}, I_{Ks}, I_{Kr}, I_{to}, and I_{CaL} between the LA and the PV based on data from dogs (7) and described in Fig. 1A (maximal conductance for I_{Kr} and I_{ks} where increased by 50% and 60% respectively while I_{K1}, I_{to} and I_{CaL} where diminished by 42%, 25% and 30% respectively). Three conditions of heterogeneity were modeled: 1) all currents varied spatially according their corresponding Boltzmann function (Condition I); 2) all currents, except I_{K1}, varied (Condition II); 3) only I_{K1} varied in space (Condition III).

To investigate the effect of the heterogeneous intercellular coupling in the LA-PV junction (8) on rotor drift in combination with the ionic heterogeneities additional 50×50 mm^2 models were generated with gradients in the isotropic intercellular coupling coefficient. The intercellular coupling in those models was set to vary following a Boltzmann profile (Fig. 1) between a baseline level at the LA edge of the model (as set in all other conditions) to a 25% smaller value at the PV edge (9).

Rotors Initiation and Characterization

Rotors were initiated by cross-field stimulations and the instantaneous center of rotation was tracked by its phase singularity point (SP) in the Hilbert-transformed movies (10,11) (see Fig. S1). In the cylindrical model, two counter-rotating (opposite chirality) rotors were generated and shown to follow a similar drift dynamics. The SP of a rotor was defined as the instantaneous location toward which all the phases in space converged and automatically detected and tracked based on the point-by-point (resolution of about 1 mm) circumferential sum of neighboring phases exhibiting a monotonic progression to approximately 2π (See movie SM1 illustrating continuous detection of SP.) For controls, rotors were initiated in two separated 2D models with either homogeneous LA or PV ionic conductances (in the absence of spatial heterogeneities) and characterized by their rotation frequency, the I_{Na} gating parameters h×j (I_{Na} availability), core size as well as wavefront curvature, action potential duration (APD), wavefront conduction velocity (CV) magnitude and wavelength (WL) of excitation (12,14) determined at 70%

amplitude (Fig. S2). Those parameters are presented for the two simulations as a function of the distance from the SP (Fig. S2, panel B). The wave front and tail were identified as a continuous isopotential line. During reentry, activation maps were generated at 50% amplitude and used to obtain local CV vector maps. The WL was calculated as the distance between the tail and the front of a wave along the CV vectors (Fig. S2, Panel B).

Data Analysis

To obtain a measure of effective refractory period (ERP) at a specific stimulation cycle length (CL) we first simulated activity for 10 s to generate steady state conditions at individual cell level and then determined the stimulus strength in the tissue model at ×1.5 the minimum excitation threshold current for a 1 mm virtual pacing electrode. Measurement consisted in 10 S1 stimuli train at CL of 1000, 500 or 140 ms, followed by an S2 premature stimulus at decreasing interval. ERP value was defined as the last (shortest) S2 allowing excitation. Measurements were repeated at 6 locations across the models.

Methods used for the parameter measurements from the numerical simulations have been previously described (13,14). Spatial profiles (between the LA and the PV edges) of APD and peak sodium availability $(h\times j)_{peak}$ were obtained by averaging those parameters in time for every pixel across the model in the last 2 s of the respective 5 s simulation. Measurements of minimal diastolic potential (MDP) and maximal upstroke velocity $(dV/dt)_{max}$ followed same temporal procedure.

SUPPLEMENTARY DISCUSSION

Ventricular fibrillation in guinea-pigs isolated hearts is driven by stable rotors in the left ventricle (LV) where the outward component of I_{K1} was found to be higher than the right ventricle (RV) (15,16). At first, the predictions in the present study suggesting that rotors would stabilize at the lowest I_{K1} region seem to conflict with those previous findings, but a deeper examination reveals that the two studies are complimentary; The present study considers rotors with a core dimension of about 11 mm (Fig. S2) that extends over an area that is wider than the distance of about 5 mm in which a gradient of currents was measured in the canine posterior LA (Fig. 1) (17,18). Moreover, our simulations here focus on currents heterogeneities that are continuous and monotonic, and in the absence of any structural heterogeneity. In the guinea-pigs study on the other hand, we have no data on the transition in the density of currents other than I_{K1}, between the LV and RV, which may be present uniformity over areas larger than the core size, thus enabling the rotor's stabilization in the larger I_{K1} zone (Fig. S5). Moreover, various anatomical components, such as the papillary bundle, are likely to present additional anchoring factors further stabilizing a driving rotor.

MOVIE SM1 DESCRIPTION

A video clip illustrating the drift of counter-rotating rotors in the heterogeneous PV-LA junction toward the PV edge of the model (Condition I, see also Fig. S1). The bottom plane is a gray-scale movie of the voltage; the upper plane is the phase movie of the voltage movie. The phase movie is used for detection of the 2 SP which are projected on the voltage map below and whose time trajectory is superimposed on the voltage movie (yellow traces) and also upward in the time axis.

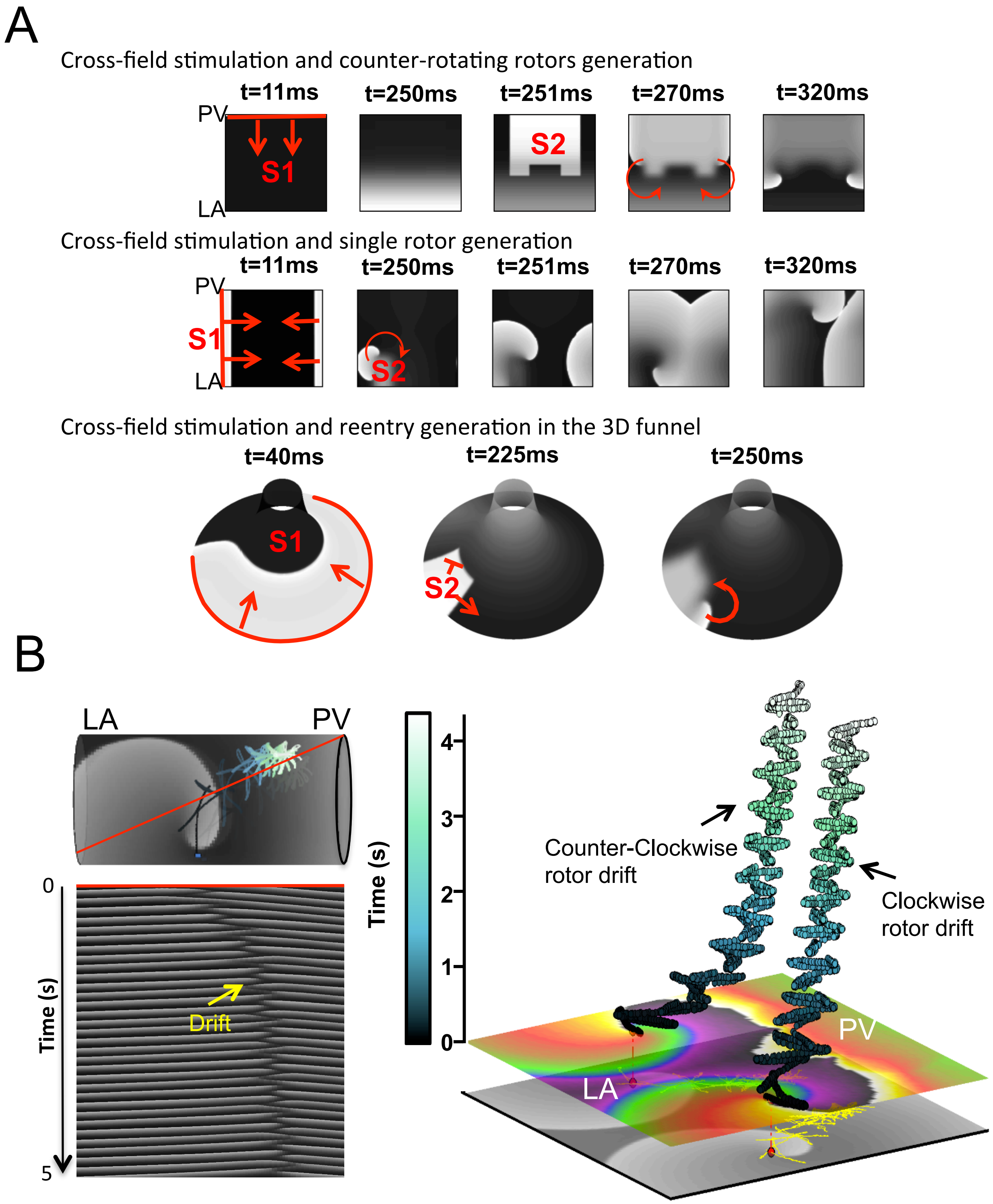

Fig. S1: Rotors initiation and tracking. A. Cross-field stimulation leading to two counter rotating or a single rotor in the cylindrical, flat and funnel-like models. Gray-scale corresponds to voltage (black, resting; white excited). Red lines: Location of S1. B. Left: Demonstration of the automatic SP tracking of a drifting rotor as the TSP (bottom) matches the SP trajectory superimposed on the cylinder model (Condition I, top). Right: In a flat model (Condition I), coexisting clockwise and counter-clockwise rotors drift toward the PV, as illustrated by the 3D TSP trajectories whose origin is at the SP in the phase map at t=0 (see movie SM1).

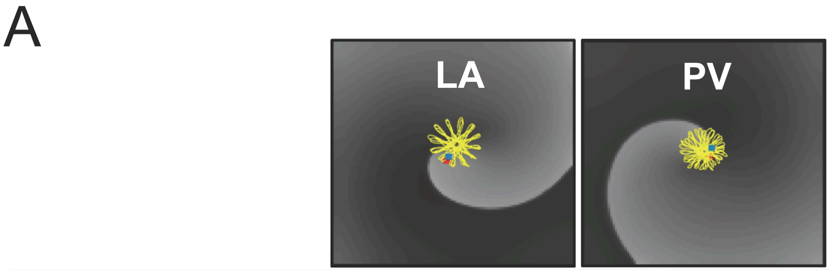

Core diameter (mm)	11.5	11.3
Rotor frequency (Hz)	7.7	7
Space and time <h×j>	0.38	0.29

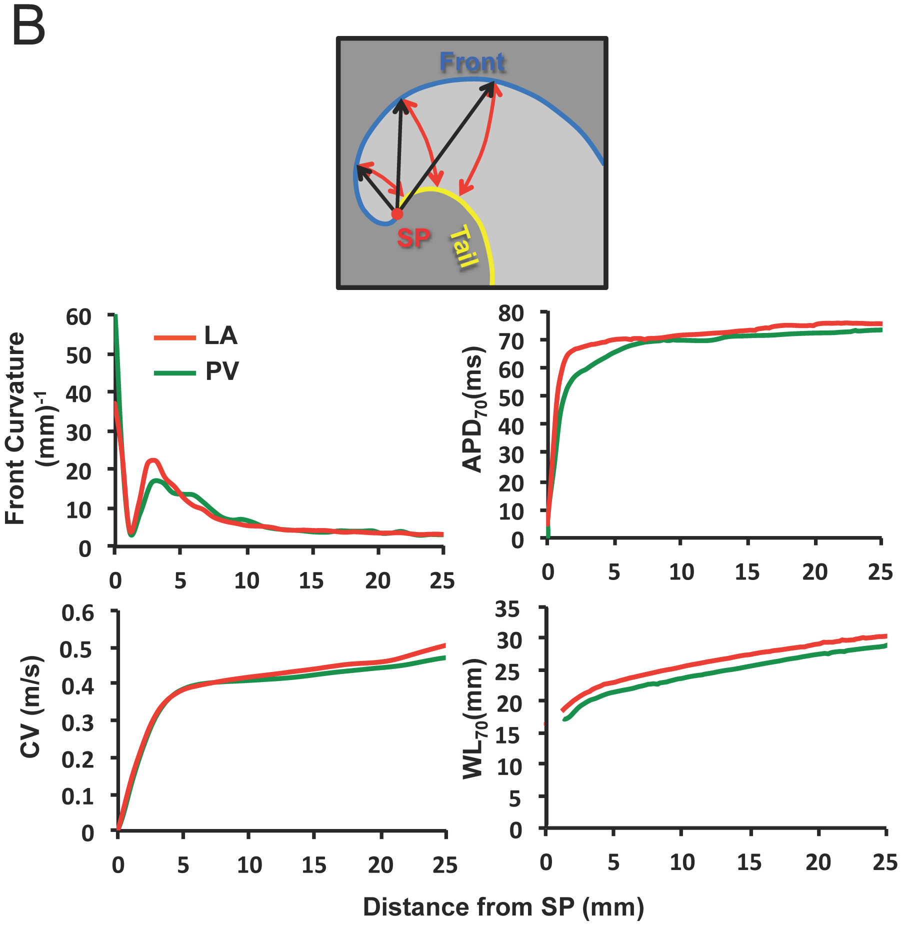

Fig. S2: Rotors characterization in homogeneous LA and PV models. The baseline relationship between the substrate and single rotor was studied in separated 2D models with homogeneous ionic conductances of the LA and PV. A. Tracking SP reveals a meandering (yellow traces), without drift, in an area of diameters of about 11.4 mm. The LA rotor was slightly faster at 7.7 Hz in comparison with PV rotor at 7 Hz, which was consistent with larger space-time averaged sodium channels availability, h·j, in the LA (0.38) than in the PV (0.29). (4) B. Top diagram illustrates the WL (red) as the distance between the isopotentials of front (blue) and tail (yellow) along the CV vectors (not shown) and distance to SP (black). Bottom graphs show rotor properties that qualitatively similar in the LA and PV, but can reach point-wise differences of up to about 20-30%.

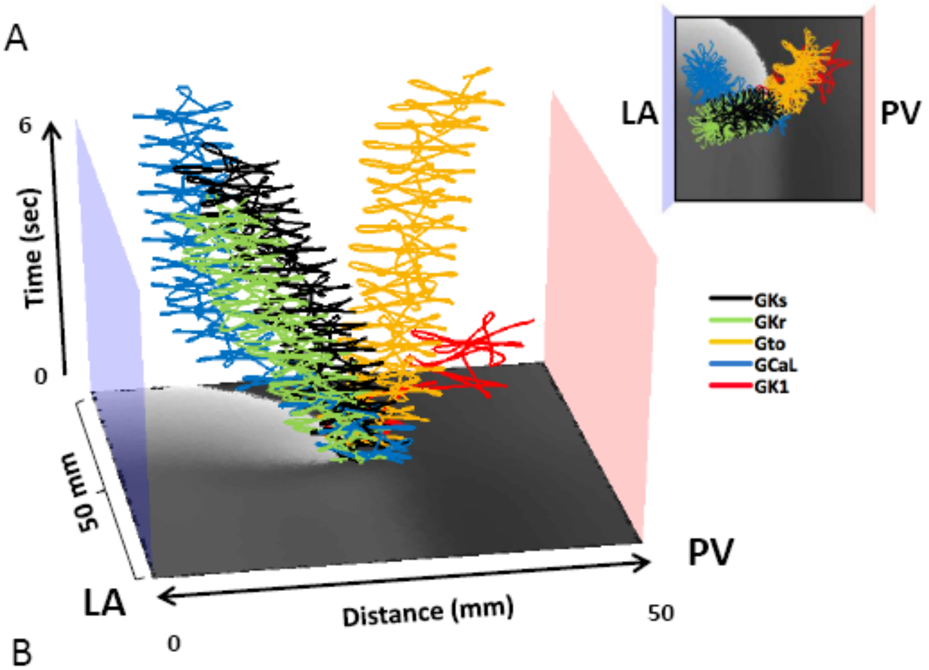

B

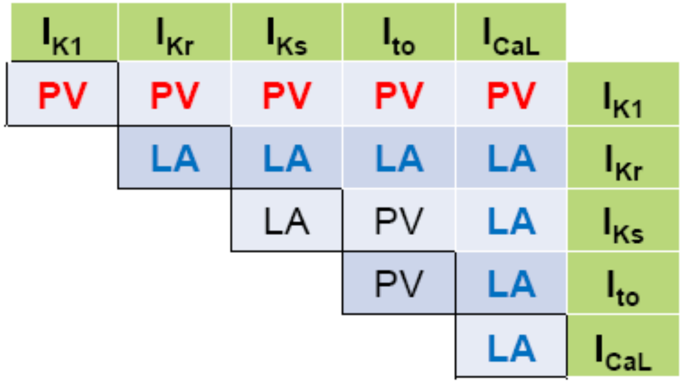

I_{K1}	I_{Kr}	I_{Ks}	I_{to}	I_{CaL}	
PV	PV	PV	PV	PV	I_{K1}
	LA	LA	LA	LA	I_{Kr}
		LA	PV	LA	I_{Ks}
			PV	LA	I_{to}
				LA	I_{CaL}

Fig. S3. Spatial gradients of individual and paired currents and reentry drift. A. Effect of spatial gradient for each individual current on rotor drift. 2D PV-LAJ model showing spatio-temporal trajectories of SPs of rotors in gradients of I_{Ks} (black), I_{kr} (green), I_{to} (yellow), I_{CaL} (blue) and I_{K1} (red) as described by the individual Boltzmann distributions in Panel A of Fig. 1. While I_{to} and I_{K1} cause the rotor to drift toward the PV edge, the gradients in the other currents cause the rotor to drift toward the opposite LA edge. Insert: top view of the trajectories. B. Effect of spatial gradients in paired currents on rotor drift. The table shows the direction of the drift when ionic gradients as indicated in the abscissa and ordinate (green cells) were considered. I_{K1} is the only current whose gradient leads to PV attraction (in red fonts) of the rotor regardless of gradient in any other current.

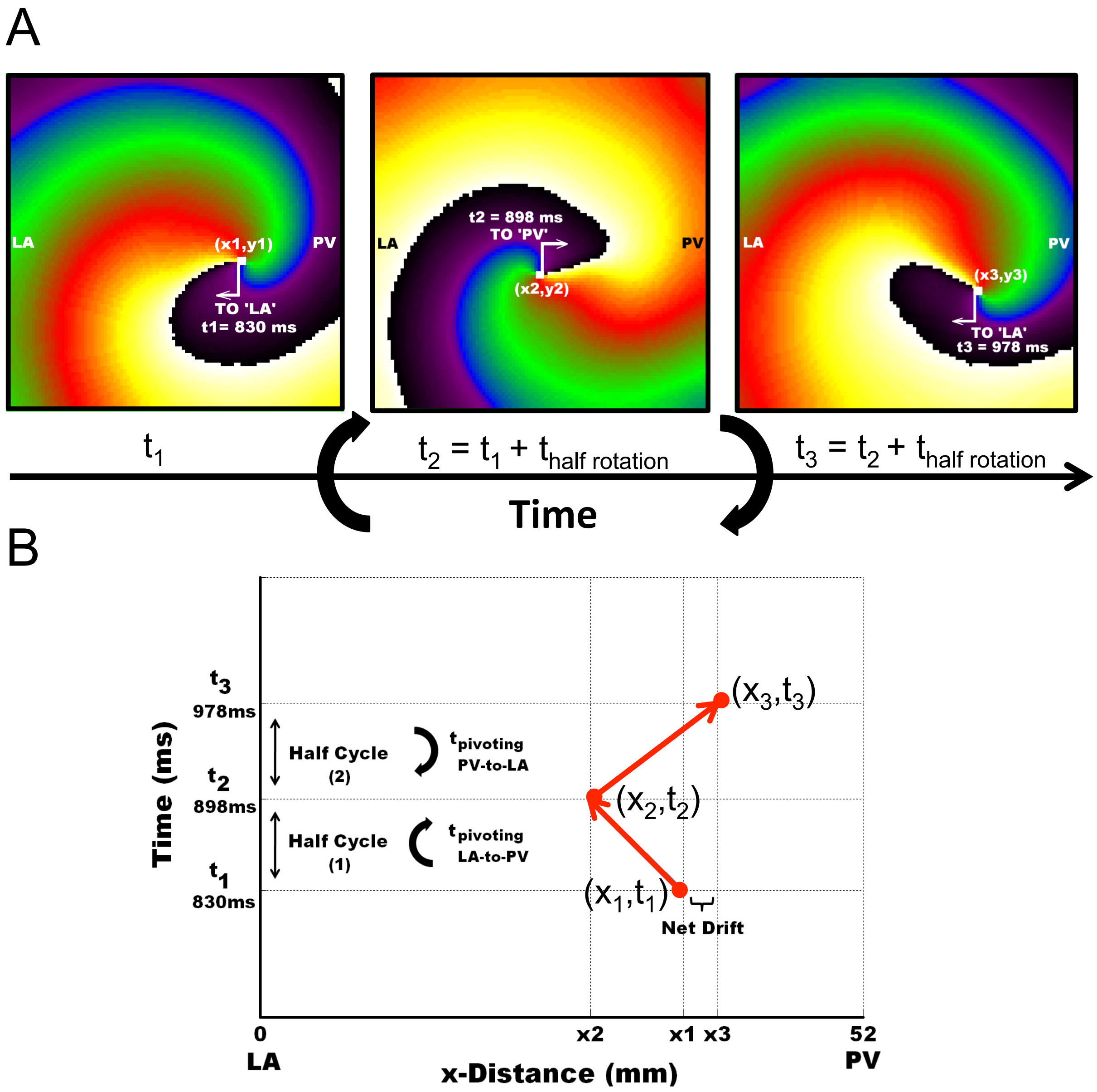

Fig. S4. Linking rotor pivoting to rotor drift. The process whereby the region with reduced excitability (h·j) attracts a rotor. A. Snapshots of the rotor at 3 moments: t_1 = 830 ms is a random reference time in which the front near the SP points toward the LA; t_2 = 898 ms is a time half a rotation later in which the front near the SP points toward the PV; t_3 = 978 ms is a time half a rotation later in which the front near the SP points again toward the LA and the rotor has completed a full rotation after t_1. The locations of the SP of the rotor at these 3 times are designated (x_1,y_1), (x_2,y_2) and (x_3,y_3), respectively. B. A time-space plot describing the trajectory of the rotor along the x direction (red arrows). The time it takes the rotor to complete its first half rotation is $t_2–t_1$=68 ms is shorter than the time it takes to rotor to complete its second half rotation $t_3–t_2$=78 ms. During that prolonged time the drift toward the PV, $(x_3 – x_2)$, is larger than the drift toward the LA, $(x_2 – x_1)$, resulting in a net drift, $(x_3 – x_1)$, toward the PV once the full rotation is completed.

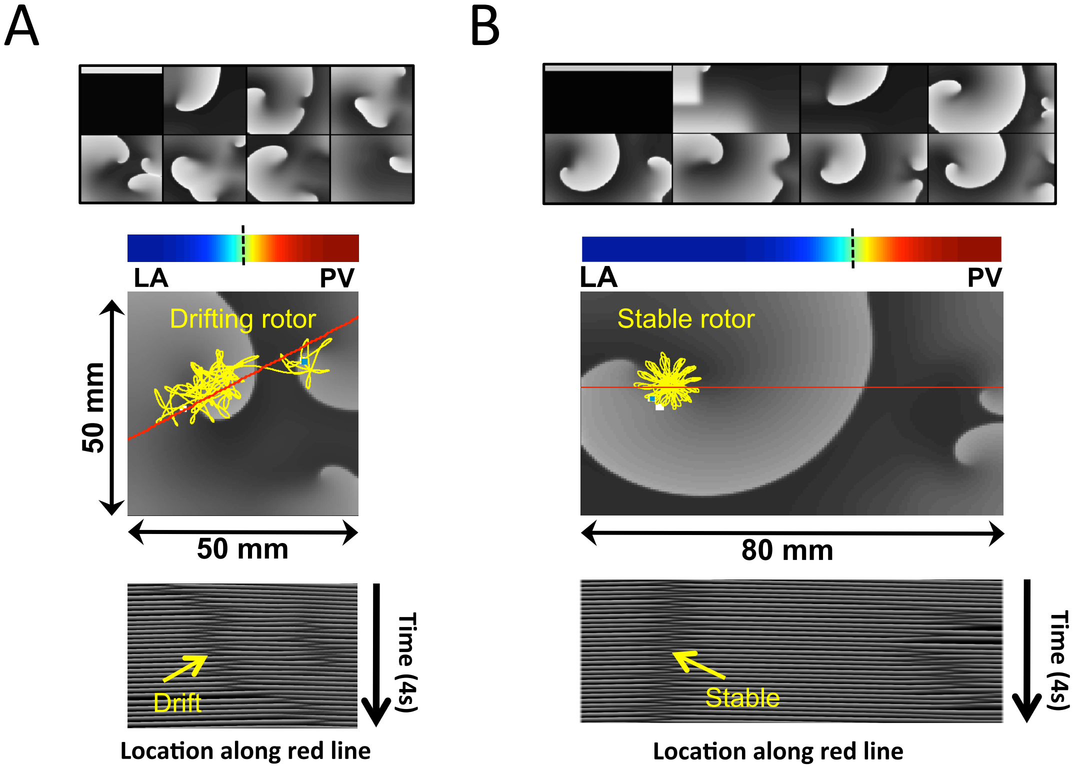

Fig. S5. Ionic gradient at the core region and rotor drifting. Here we demonstrate that heterogeneity is required within the core region to induce rotor drift. A. Simulation in a 50×50 mm^2 model of the PV-LAJ whose Boltzmann distribution is varying throughout the model (Condition I). B. Simulation in a 80×50 mm^2 model of the PV-LAJ whose Boltzmann distribution is mostly uniform in the LA portion of the model. Top panels: Sequential voltage snap shots (left to right and top to bottom) of the spontaneous time-course of a rotor initiated in the LA portion of the model. Color bars: The normalized Boltzmann factor variation from the LA (blue, 0) to the PV (red, 1) edges (see Fig. 1). The dash vertical line illustrates the steepest gradient location. It is appreciated that there is a large area in the LA portion of the model in B that is uniformly zero (blue). The time-space plots (bottom) taken along the red lines of the models show that the core size (vertical dark gray band) is smaller than the area with LA uniform conditions in B, but not so in A, enabling a stable rotor in LA region, without a drift, in B but not in A. The appearance of a stable LA rotor in B is consistent with the stable rotor demonstrated recently by Campbell et al in a 35-mm wide monolayer of cardiomyocytes with a relatively more step-wise heterogeneity in I_{Kr} expression (Boltzmann Δx of about 1 mm compared to 5 mm in the present study) (12).

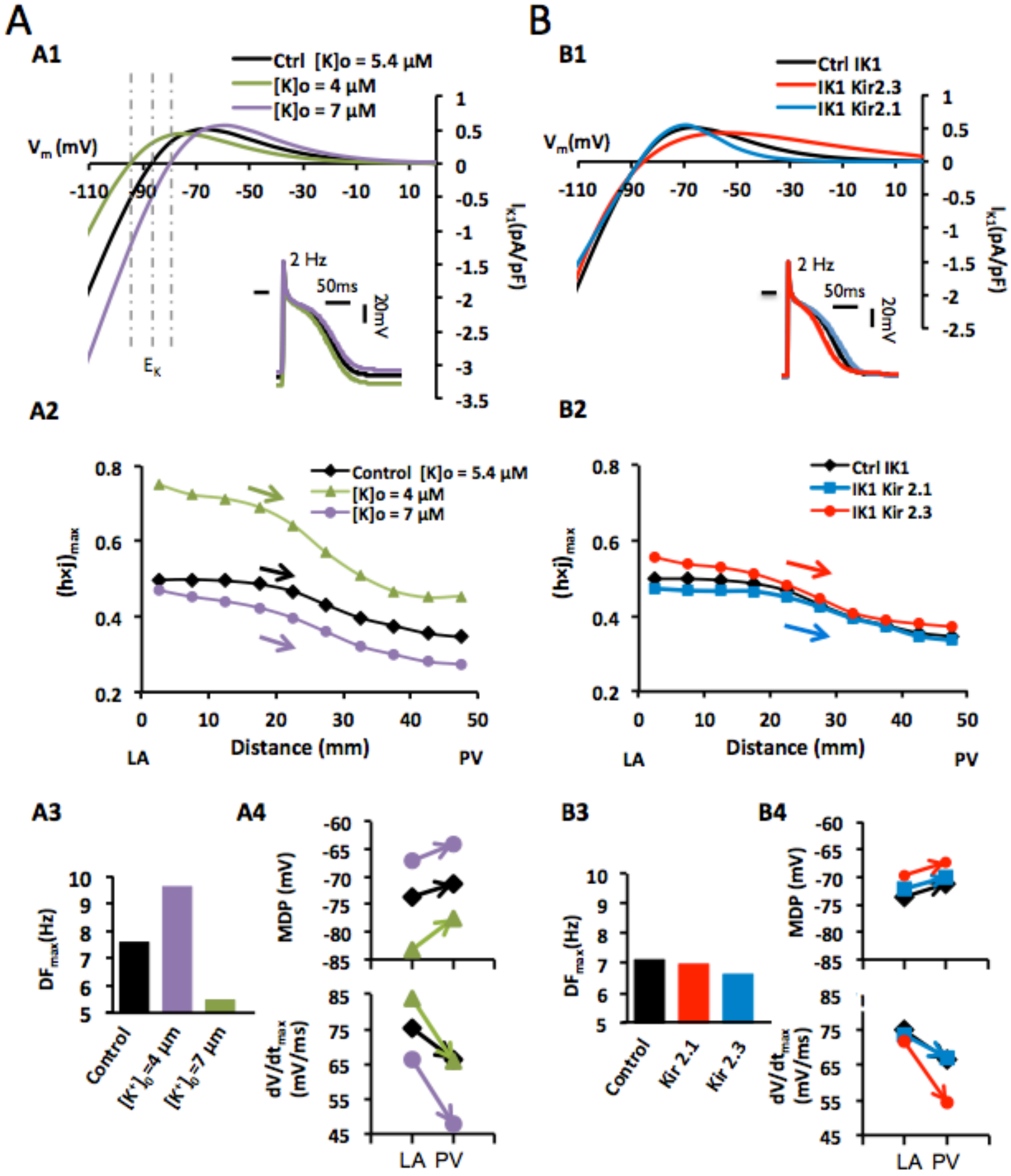

Fig. S6. Effect of $[K]_o$ and major I_{K1} isoforms on rotor drift direction. A. Investigating the effect of $[K]_o$ on rotor drift. A1. I_{K1} I-V curves under conditions of normal, reduced and increased $[K]_o$ demonstrate shifting of the reversal potential and altering slope resistance as well as outward current properties. A2. Rotors drifted toward the excitability sink (lowest h×j) at the PVs for all $[K]_o$ levels. A3. Effect of $[K]_o$ on DF_{max}. A4. Both MDP and dV/dt_{max} measured during rotor activity were consistent predictors of rotor drift for all $[K]_o$ levels. B. Investigating the effect of changes in I-V relationship of I_{K1} resulting from altering its isoforms. B1. I_{K1} I-V profiles for a typical Kir2.1 and Kir2.3 dominant isoforms. B2. As in panel A2, rotor is drifting toward the excitability sink (lowest h×j) in the PV edge for any I-V profile. B3. Effect of the different I-V profiles in B1 on DF_{max} is small. B4. Both MDP and dV/dt_{max} measured during rotor activity were consistent predictors of rotor drift for all I-V profiles tested.

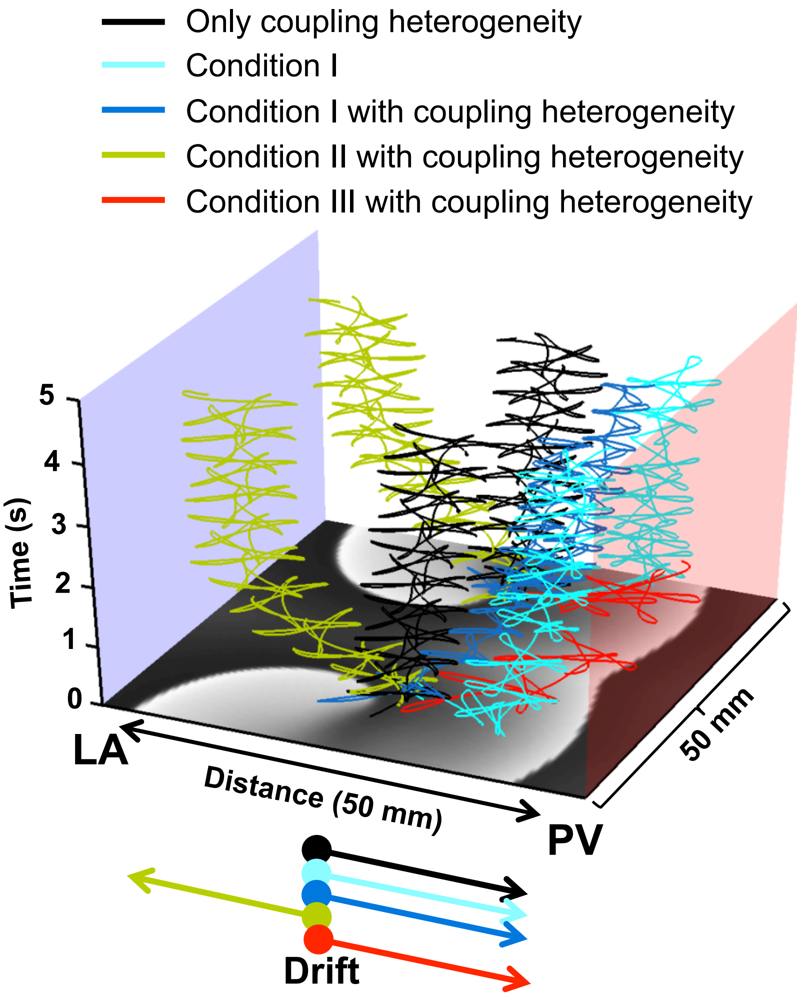

Fig. S7. Heterogeneous intercellular coupling in the PV-LAJ and rotor drift. Models were generated with heterogeneous isotropic intercellular coupling following a Boltzmann profile with 25% reduction in the PV vs. the LA edges. The figure shows a TSP and drift directions of counter-rotors at the various conditions indicated. In the presence of only coupling heterogeneity the rotors drift toward the PV (black) less than the drift with all ionic gradients (Cyan, Condition I). The drifts in the models with heterogeneous coupling combined with either Conditions I, II and III did not differ qualitatively from those with a uniform coupling (see Fig. 2) suggesting that the presence of the heterogeneous coupling does not alter the major role of I_{K1} in determining the rotor drift direction in the PV-LAJ toward the PV edge, where the coupling coefficient is lowest.

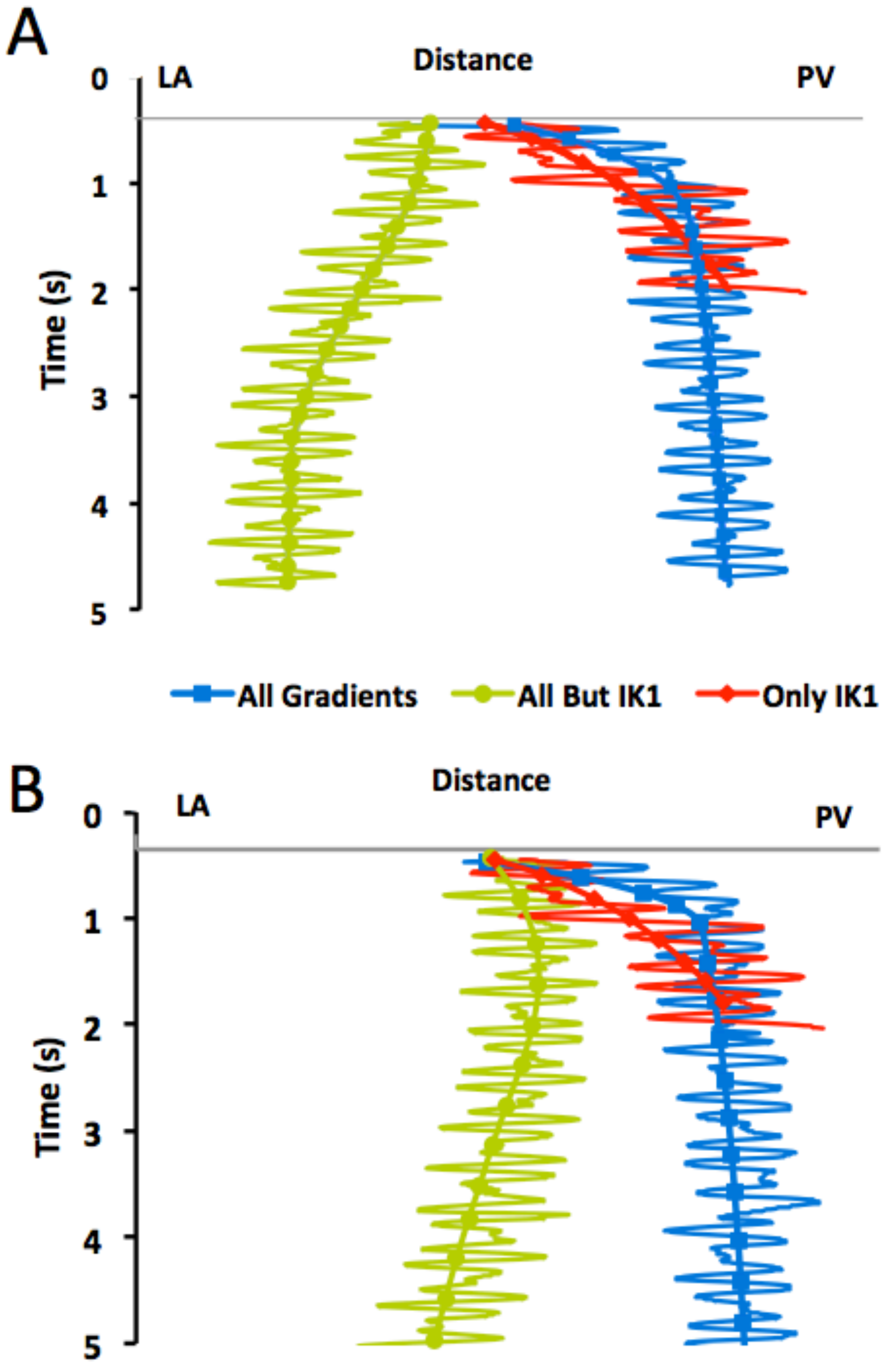

Fig. S8. Rotor drift in the presence of additional gradient in sodium current. The presence of I_{Na} gradients in the PV-LAJ is suspected but not yet confirmed. Thus we investigate its role in determining drift direction relative to I_{K1} gradient role. Gradients in I_{Na} whereby the PV conductance was reduced by 20% (panel A) and 40% (panel B) were incorporated in models similar to those used in Fig. 2. The TSPs here show SP trajectory for the 2 conditions of gradients in all currents (All Gradients; Condition I + gradient in I_{Na}; blue traces) and gradients in all currents, but I_{K1} (All but I_{K1}; Condition II + gradient in I_{Na}; green traces), as well as the gradient only in I_{K1} (Condition III; Only I_{K1}; red traces). Both panels show evolution of the tip trajectories for the rotors similar to those presented in Fig. 2, demonstrating that while I_{Na} contributes to the drift of the rotors in the PV-LAJ, I_{K1} is still the dominant current whose gradient determines drift direction.

SUPPLEMENTAL REFERENCE LIST

1. Wozniak-Skowerska, I., M. Skowerski, A. Wnuk-Wojnar, A. Hoffmann, S. Nowak, A. Gola, M. Sosnowski, and M. Trusz-Gluza. 2011. Comparison of pulmonary veins anatomy in patients with and without atrial fibrillation: analysis by multislice tomography. Int. J. Cardiol. 146: 181-185.
2. Courtemanche, M., R. J. Ramirez, and S. Nattel. 1998. Ionic mechanisms underlying human atrial action potential properties: insights from a mathematical model. American Journal of Physiology-Heart and Circulatory Physiology 44: H301-H321.
3. Kneller, J., R. Zou, E. J. Vigmond, Z. Wang, L. J. Leon, and S. Nattel. 2002. Cholinergic atrial fibrillation in a computer model of a two- dimensional sheet of canine atrial cells with realistic ionic properties. Circ. Res. 90: E73-E87.
4. Pandit, S. V., O. Berenfeld, J. M. Anumonwo, R. M. Zaritski, J. Kneller, S. Nattel, and J. Jalife. 2005. Ionic determinants of functional reentry in a 2-D model of human atrial cells during simulated chronic atrial fibrillation. Biophys. J. 88: 3806-3821.
5. Dhamoon, A. S., S. V. Pandit, F. Sarmast, K. R. Parisian, P. Guha, Y. Li, S. Bagwe, S. M. Taffet, and J. M. Anumonwo. 2004. Unique Kir2.x properties determine regional and species differences in the cardiac inward rectifier K+ current. Circ. Res. 94: 1332-1339.
6. Clayton RH, Zhuchkova E.A., Panfilov AV. 2005. Phase singularities and filaments: Simplifyingg complexity in computational models of ventricular fibrillation. Progress in Biophysics and Molecular Biology 90 (2006) 378-398
7. Cha, T. J., J. R. Ehrlich, L. Zhang, D. Chartier, T. K. Leung, and S. Nattel. 2005. Atrial Tachycardia Remodeling of Pulmonary Vein Cardiomyocytes: Comparison With Left Atrium and Potential Relation to Arrhythmogenesis. Circulation 111: 728-735.
8. Chaldoupi, S. M., P. Loh, R. N. Hauer, J. M. de Bakker, and H. V. van Rijen. 2009. The role of connexin40 in atrial fibrillation. Cardiovasc. Res. 84: 15-23.
9. Verhuele S, Wilson EE, Arora R., Engle SK., Scott LR., Olgin JE 2002. Tissue structure and connexin expression of canine pulmonary veins. Cardiovasc. Res. 55: 727-738.
10. Zlochiver, S., M. Yamazaki, J. Kalifa, and O. Berenfeld. 2008. Rotor meandering contributes to irregularity in electrograms during atrial fibrillation. Heart Rhythm 5: 846-854.
11. Zlochiver, S., V. Munoz, K. L. Vikstrom, S. M. Taffet, O. Berenfeld, and J. Jalife. 2008. Electrotonic myofibroblast-to-myocyte coupling increases propensity to reentrant arrhythmias in two-dimensional cardiac monolayers. Biophys. J 95: 4469-4480.
12. Noujaim, S. F., S. V. Pandit, O. Berenfeld, K. Vikstrom, M. Cerrone, S. Mironov, M. Zugermayr, A. N. Lopatin, and J. Jalife. 2007. Up-regulation of the inward rectifier K+ current (I K1) in the mouse heart accelerates and stabilizes rotors. J. Physiol 578: 315-326.
13. Hou, L., M. Deo, P. Furspan, S. V. Pandit, S. Mironov, D. S. Auerbach, Q. Gong, Z. Zhou, O. Berenfeld, and J. Jalife. 2010. A major role for HERG in determining frequency of reentry in neonatal rat ventricular myocyte monolayer. Circ. Res. 107: 1503-1511.
14. Campbell, K., C. J. Calvo, S. Mironov, T. Herron, O. Berenfeld, and J. Jalife. 2012. Spatial gradients in action potential duration created by regional magnetofection of hERG are a substrate for wavebreak and turbulent propagation in cardiomyocyte monolayers. J. Physiol 590: 6363-6379.

15. Warren, M., P. K. Guha, O. Berenfeld, A. Zaitsev, J. M. B. Anumonwo, A. S. Dhamoon, S. Bagwe, S. M. Taffet, and J. Jalife. 2003. Blockade of the inward rectifying potassium current terminates ventricular fibrillation in the guinea pig heart. J. Cardiovasc. Electrophysiol. 14: 621-631.
16. Samie, F. H., O. Berenfeld, J. Anumonwo, S. F. Mironov, S. Udassi, J. Beaumont, S. Taffet, and J. Jalife. 2001. Rectification of the Background Potassium Current: A Determinant of Rotor Dynamics in Ventricular Fibrillation. Circ Res 89: 1216-1223.
17. Ehrlich, J. R., T. J. Cha, L. M. Zhang, D. Chartier, P. Melnyk, S. H. Hohnloser, and S. Nattel. 2003. Cellular electrophysiology of canine pulmonary vein cardiomyocytes: action potential and ionic current properties. Journal of Physiology-London 551: 801-813.
18. Cha, T. J., J. R. Ehrlich, L. Zhang, D. Chartier, T. K. Leung, and S. Nattel. 2005. Atrial Tachycardia Remodeling of Pulmonary Vein Cardiomyocytes: Comparison With Left Atrium and Potential Relation to Arrhythmogenesis. Circulation 111: 728-735.